

Time-Resolved Surface Heat Flux Measurements in the Wing/Body Junction Vortex

D. J. Lewis,* R. L. Simpson,† and T. E. Diller‡

Virginia Polytechnic Institute and State University, Blacksburg, Virginia 24061

Time- and spatially-resolved heat flux measurements are reported for the endwall surface in the turbulent, incompressible flow in the nose region of a wing-body junction formed by a wing and a flat plate. Both the wing and the flat plate were heated and held at a constant and uniform temperature. The effects of cylindrical wing geometry on heat flux were investigated by taking heat flux measurements in the nose regions of a 3:2 elliptic nose/NACA 0020 tail shape, a circular cylinder with a wedge tail, and an NACA 0015. Heat flux rates were increased up to a factor of 3 over the heat flux rates in the approach boundary layer. The rms of the heat flux fluctuations were as high as 25% of the mean heat flux in the vortex-dominated nose region. Away from the wing, upstream of the time-averaged vortex center, augmentation in the heat flux is due to increased turbulent mixing caused by large-scale unsteadiness of the vortex. A new three-dimensional extension of an existing correlation is proposed to account for the effects of the horseshoe vortex on heat transfer in this region. Adjacent to the wing the augmentation in heat flux is due to a change in the mean velocity field.

Nomenclature

C_p	= specific heat
E	= output voltage of gauge
f	= frequency, Hz
$G_{qq}(f)$	= auto spectral density function of q'
h	= convection film coefficient, $q/(T_g - T_\infty)$
k	= turbulent kinetic energy
Pr	= Prandtl number
q	= time-mean heat flux
q'	= fluctuating component of heat flux
$Re_{()}$	= Reynolds number based on ()
S	= heat flux gauge sensitivity
St	= Stanton number, $h/(\rho C_p U_{ref})$
St'	= Stanton prime correlation, $h/(\rho C_p u_{rms,max})$
T	= temperature
T_f	= film temperature, $(T_g + T_\infty)/2$
T_g	= gauge surface temperature
T_∞	= temperature of freestream air
t	= maximum thickness of a given wing
U, V, W	= time-averaged velocity components in x, y, z directions, respectively
U_{ref}	= freestream velocity
u, v, w	= fluctuating velocity components in x, y, z directions, respectively
x, y, z	= Cartesian coordinate system axis
x_{lois}	= distance measured along line of symmetry of wing from wing leading edge to line of low shear
x_{sep}	= distance measured along line of symmetry of wing from wing leading edge to line of separation
ΔT	= temperature difference, $T_g - T_\infty$
η_g	= gauge emissivity
θ	= momentum thickness
ρ	= density

σ = Stefan Boltzmann constant,
 $5.67 \times 10^{-8} \text{ W}/(\text{m}^2 \text{ K}^4)$

Subscripts

rms = root mean square of fluctuating component
rms,max = maximum rms value of fluctuating component present in the boundary layer at a given x, z location

Introduction

A WING/BODY junction flow is formed when the boundary layer on a surface encounters the blunt nose of an airfoil-shaped body or strut protruding from that surface. When the approach boundary layer encounters the wing, it separates in front of the nose and the separation line stretches around the sides of the wing. Closer to the nose a horseshoe vortex forms that stretches around the body. A simplified schematic of the horseshoe vortex system is illustrated in Fig. 1. The junction vortex system is of interest in many practical engineering applications. This flow pattern is present at aircraft wing roots, ship and submarine appendage/hull junctions, in gas turbines at the blade/hub junction, and in flows with injection normal to the mean flow.

The flowfield in the wing/body junction is dominated by large-scale, aperiodic motions. Devenport and Simpson¹ measured velocities in the plane of symmetry upstream of a wing/body junction and observed bimodal (double peaked) velocity probability histograms. Further research showed that the flow at a given point in this zone switched aperiodically from one mode to the other. This double-peaked structure has also been found in histograms of pressure fluctuation measurements^{2,3} made on the endwall upstream of a wing/body junction. Hydrogen bubble flow visualizations by Kim et al.,⁴ revealed that the aperiodic motions were caused by stretching of the horseshoe vortex about the wing and by interaction of the horseshoe vortex with corotating separation vortices that form between the horseshoe vortex and the line of separation. This aperiodic phenomenon is responsible for the observed high turbulence intensities and high surface pressure fluctuations and may be responsible for high heat transfer rates. This is of great importance to gas turbine heat transfer, where hub and casing boundary layers produce large heat transfer rates at the junctions with blades.

Few studies of the effects of the horseshoe vortex on end-wall heat flux have been made. Time-averaged heat flux measurements in turbine cascades have been made by several

Received Aug. 4, 1993; revision received Feb. 4, 1994; accepted for publication Feb. 7, 1994. Copyright © 1994 by the authors. Published by the American Institute of Aeronautics and Astronautics, Inc., with permission.

*Research Assistant, Department of Aerospace and Ocean Engineering. Student Member AIAA.

†Jack E. Cowling Professor, Department of Aerospace and Ocean Engineering. Fellow AIAA.

‡Professor, Department of Mechanical Engineering. Member AIAA.

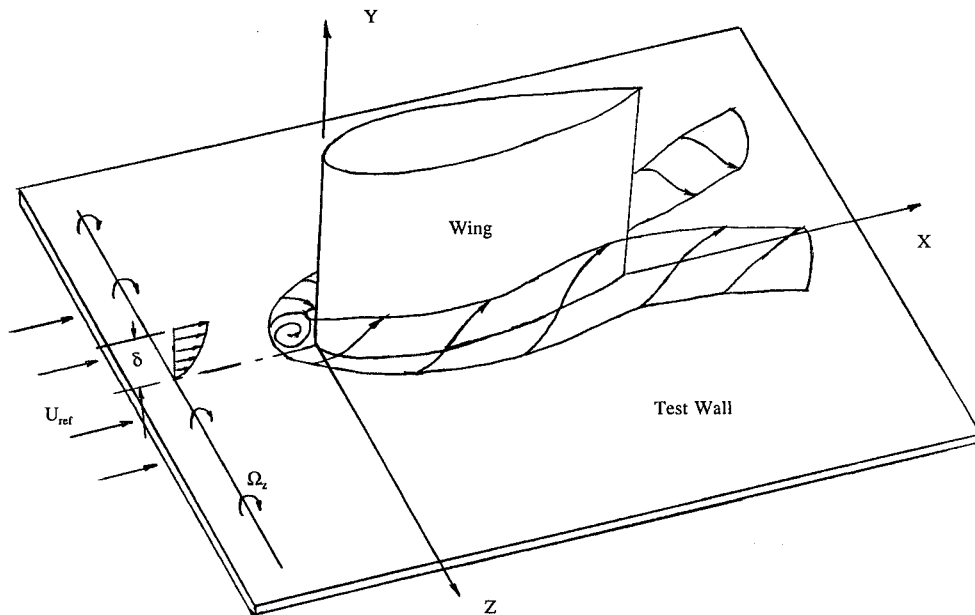


Fig. 1 Sketch of the wing-body junction showing the horseshoe vortex and the tunnel coordinate system.

researchers. Blair⁵ and Dunn and Stoddard⁶ measured end-wall heat flux rates between blades in a turbine cascade and found that the horseshoe vortex increased heat flux by a factor of 3 near the leading edge of the turbine/endwall junction.

The effects of the approach boundary-layer thickness on heat flux to the endwall in turbine cascades have been investigated with inconclusive results. Grazianni et al.⁷ found that minimum and maximum Stanton number levels were independent of the approach boundary-layer thickness. Grazianni et al. also found that the area of influence of the horseshoe vortex was increased with increasing approach boundary-layer thickness. In contrast, Georgiou et al.⁸ found that the effect of reducing the inlet boundary-layer thickness was to uniformly increase the local heat flux rate, but that the shape of the iso-heat-transfer contours were unaffected by boundary layer thickness. Georgiou et al. also found changes in free-stream turbulence levels to have only a minimal effect on heat flux rates in the horseshoe vortex.

Gaugler and Russell⁹ compared their measured turbine/endwall heat flux rates with flow visualizations of Hylton et al.¹⁰ The only obvious correlation between the horseshoe vortex and endwall heat flux was found near the vane leading edge where a local peak in heat flux occurred. The three-dimensional separation line was found to not correlate with any endwall heat flux features. Hippensteele and Russell¹¹ measured turbine/endwall heat flux rates using high spatial resolution liquid crystal sheets for the same turbine cascade used by Gaugler and Russell and obtained similar results.

Only recently have time-resolved heat flux measurements been made in the junction vortex. A high-frequency-response heat flux gauge called the Heat Flux Microsensor was recently used by Swisher et al.¹² to measure time-resolved endwall heat flux along the stagnation streamline upstream of a streamlined cylinder. The rms of the heat flux unsteadiness was found to be as high as 30% of the mean heat flux in the horseshoe vortex.

All of the previous studies have shown similar levels and patterns of wing/endwall heat flux. High levels of heat flux were found in the horseshoe vortex with peak levels occurring near the wing. Freestream turbulence and approach boundary-layer thickness have been found to have little effect on heat flux to the endwall, but these effects are still poorly understood. The relationship between the fluid dynamics and the heat flux has not been established.

The objective of this article is to relate the turbulent heat flux to the fluid dynamics in a horseshoe vortex. No attempt

is made here to predict the fluid dynamics because this has been the subject of many previous papers. It will therefore be assumed that the fluid dynamics (location and strength of the vortex) are known and the heat flux will be related to these parameters. The primary model chosen for this work was the 3:2 semielliptic nosed/NACA 0020 tailed airfoil for which Devenport and Simpson¹ have made detailed 3-component laser Doppler velocimetry (LDV) measurements.

Here we report detailed time- and spatially-resolved heat flux measurements that are necessary to understand the effects of the horseshoe vortex on the heat flux. We examine the effects of turbulence on heat flux and determine if the bimodal velocity phenomenon is responsible for the augmentation in the surface heat flux. Results for several different wing shapes also are presented to examine the effects of wing geometry.

Experimental Apparatus and Procedure

Test Facility

The wind tunnel is an open-circuit type and is powered by a centrifugal blower. Air from the blower is supplied to the test section after passing through a fixed-setting damper, a plenum, a section of honeycomb, seven screens which are used to remove much of the turbulence intensity, and a 4:1 contraction nozzle to further reduce the turbulence and to accelerate the flow to test speed. The potential core of the flow entering the test section is uniform to within 0.5% in the spanwise direction and 1% in the vertical direction with a turbulence intensity of 0.1% at 27 m/s.¹

Figure 2 is a side view of the 6-m-long and 0.91-m-wide test section. The upper wall is made from Plexiglas[®] reinforced with aluminum channel. The glass side walls are lined internally with removable 6.4-mm-thick Plexiglas sheets. The lower wall is made from 19-mm-thick fin-form plywood. Flow entering the test section is subjected to a further 1.5:1 contraction produced by the shape of the upper wall. A throat is reached 1.63 m downstream of the entrance where the section is 254 mm in height. Downstream of the throat the upper wall is almost parallel to the flat lower wall, diverging gradually from it with distance downstream to account for boundary-layer growth.

In order to create a new fluid boundary layer at the beginning of the heat flux surface, a heated false floor was placed in the tunnel and a suction slot was opened in the tunnel floor as shown in Fig. 2. The upstream boundary layer formed on

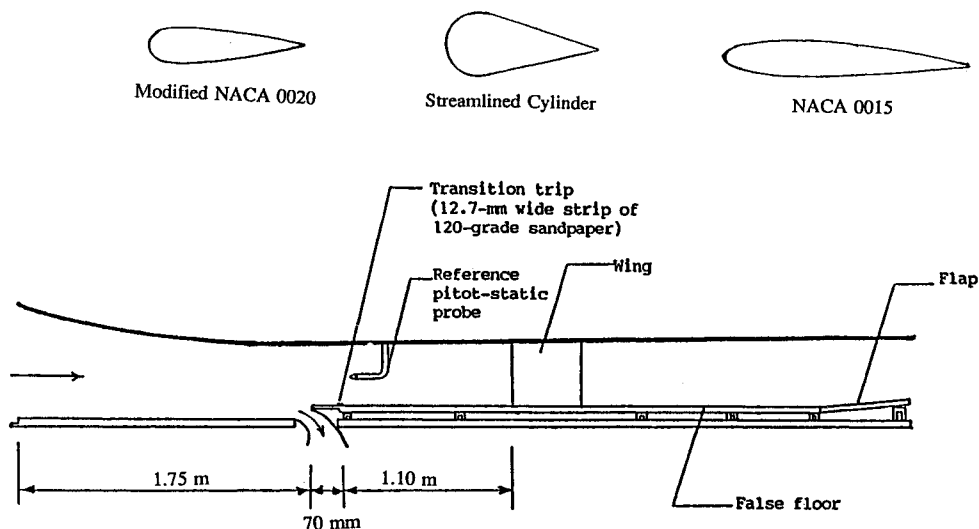


Fig. 2 Side view of the boundary-layer tunnel test section with heated false floor and wing shapes.

the tunnel floor is sucked out through the slot and a new boundary layer develops from the rounded leading edge of the false floor. The thin boundary layer is tripped by a 12.7-mm-wide strip of 120-grade sandpaper, located with its leading edge 70 mm downstream of the false floor leading edge. This is the same arrangement used by Ölçmen and Simpson.² The forward edge of the suction slot is located 145 mm downstream of the throat of the test section. The false floor rests with its upper surface 35 mm above the tunnel floor and its leading edge 116 mm downstream of the throat. The false floor was made of 3 sections of 1.59-cm-thick aluminum plate. A trailing-edge flap set at an angle of 7 deg was used to produce a constant static pressure on the tunnel floor throughout the heated test section.

The wing was mounted in the test section at zero incidence and sweep with its leading edge 1.17 m downstream of the leading edge of the false floor. Since the measurements were made only with the wing at a zero angle of attack, it was possible to reduce blockage-induced pressure gradients by contouring the side walls of the wind tunnel to approximately follow the streamlines produced by the 3:2 elliptic nose/NACA 0020 tailed wing in unbounded potential flow. This was accomplished by removing the 6.4-mm-thick Plexiglas sheets that line the tunnel sidewalls from the region surrounding the wing. This effectively increased the width of the test section by 12.7 mm from a location 330 mm upstream of the wing leading edge to another 203 mm downstream of its trailing edge. The abrupt corners at the edges of the liner were faired over using adhesive tape. This same arrangement was used for all wing shapes.

Streamwise velocity measurements were made using a hot-wire anemometer to determine the cold wall approach boundary-layer conditions. The approach boundary-layer velocity profile was measured 21.58 cm in front of the leading edge of the 3:2 elliptic nose/NACA 0020 tailed wing with the model in place. The nominal freestream velocity was 32.34 m/s with a Reynolds number based on momentum thickness of 3730. The momentum thickness was 1.9 mm and the displacement thickness was 2.6 mm. The friction velocity was estimated to be 1.32 m/s.

The aluminum false floor was heated and held at a constant and uniform temperature. Silicone-rubber-insulated electric resistance heaters were held against the bottom of the false floor by 1.9-cm-thick styrofoam sheet which was secured by bolts. T-type thermocouples were soldered into 3.18-mm-diam brass tube and press fit into the aluminum floor for feedback control. Power to the heaters was controlled by 5, Eurotherm 810, 3-mode process controllers, each connected to a Eurotherm 831 SCR power supply. Because of the high thermal conductivity of aluminum and the thickness of the false floor,

the surface was nearly isothermal. The automatic controllers held the surface temperature constant and uniform to within $\pm 0.5^\circ\text{C}$. The location of a "virtual origin" was calculated from the momentum thickness using the correlation for turbulent boundary layers given by Kays and Crawford¹³:

$$(\theta/x) = 0.036Re_x^{-0.2} \quad (1)$$

The virtual origin was 1 cm downstream of the leading edge of the false floor. The unheated starting length was approximately 5 cm, and was therefore negligible.

The heat flux probe was mounted in a cam system installed in the false floor in front of the wing. The cams were made of 1.59-cm-thick aluminum plate and were heated from beneath by electric resistance heaters. Rotating one or both cams allowed the probe to be positioned throughout a 12.7-cm-radius region in front of the wing. The cam system is illustrated in Fig. 7 of Lewis et al.¹⁴

Wing Shapes

The wing shapes used were a modified NACA 0020 tailed wing, a streamlined cylinder shape, and an NACA 0015. The modified NACA 0020 wing consists of a 3:2 elliptical nose (with its major axis aligned with the chord) and an NACA 0020 tail joined at the maximum thickness. These wing shapes were chosen because of the bimodal surface pressure fluctuation phenomenon observed by Ölçmen and Simpson² for these wing shapes. The height of each model was 22.9 cm, which spanned the test section. The models were each made of aluminum and were heated with silicone-rubber-insulated electric resistance heaters glued inside the models. Each model was positioned in the same location in the tunnel with its leading edge 1.17 m from the leading edge of the false floor. The flow over each model was tripped with a strip of 120-grade sandpaper to prevent unsteadiness due to natural flow transition. The length, maximum thickness, trip width, and trip location of each wing shape are given in Table 1. Results from oil flow visualizations made by Ölçmen and Simpson on the false floor in front of each wing are also given in Table 1. These oil visualizations revealed the location of primary separation of the approach boundary layer x_{sep} and the location of a second line, closer to the model which Devenport and Simpson¹ have shown to mark the location of minimum local streamwise shear x_{lots} measured from the wing leading edge along the line of symmetry in front of each wing. These lines are illustrated in Fig. 3.

Heat Flux Measurement

Heat flux measurements were made using both a high-frequency-response, low output gauge and a high sensitivity gauge.

Table 1 Characteristic dimensions of the wing models and results from oil flow visualization

Model name	Chord length, cm	Maximum thickness, cm	Trip location/chord, circumferential	Trip length/chord	x_{sep}^a , cm	x_{tols}^a , x/x_{sep}
Modified NACA 0020	30.5	7.17	0.1406	0.0208	3.23	0.60
Streamlined cylinder	29.8	12.70	0.2542	0.0374	6.59	0.53
NACA 0015	60.8	9.21	0.1152	0.0376	2.71	0.53

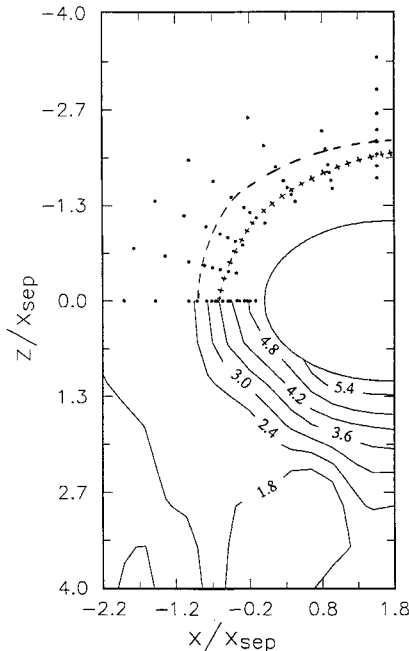
^aFrom Ref. 2.

Fig. 3 Contours of constant time-mean Stanton number $\times 10^3$ for the modified NACA 0020 wing; ---, line of separation; + + + +, line of low shear; •, locations of heat flux measurements. Line 1 is along the line of symmetry, with lines 2–7 proceeding clockwise around the wing.

The high-frequency-response gauge was a Heat Flux Microsensor manufactured by Vatel Corp. Similar gauges have been used in several other studies of turbulent heat flux.^{12,15} The Heat Flux Microsensor is a layered-type gauge that operates by relating the heat flux to the measured temperature drop across a thin thermal resistance layer. A detailed description of the Microsensor construction can be found in Hager et al.¹⁶ The Microsensor has a flat frequency response up to 50 kHz¹⁷ and outputs a voltage directly proportional to the heat flux. The gauge was calibrated by measuring the heat flux rate at a three-dimensional stagnation point where the heat flux coefficient had been previously determined. The gauge sensitivity was found to be $66 \pm 10 \mu\text{V}/(\text{W}/\text{cm}^2)$.¹⁸ The thin construction of the gauge ($<2 \mu\text{m}$) is physically unobtrusive in the flow and causes minimal disruption of the thermal boundary layer due to a step change in temperature. The sensing area of the gauge is $3 \times 3 \text{ mm}$. Two 0.076-mm-diam type-T thermocouples were mounted in the surface of the gauge and the floor to match the gauge surface temperature with the temperature of the heated floor.

The output voltage of the Microsensor was amplified by a differential dc-powered amplifier designed and built by Vatel Corp. The signal was amplified by a gain of 1000 and connected to a Hewlett Packard 3562A Dynamic Signal Analyzer. The signal was sampled at a frequency of 10,240 Hz. One hundred loads of 2048 samples were taken over a period of approximately 1 min and recorded on floppy disk.

Due to the low output voltage of the Microsensor, a second, high-sensitivity Schmidt-Boelter gauge manufactured by

Medtherm Corp. (model 8-2-.625-36-20893T) was used to measure the mean time-averaged heat flux. The Schmidt-Boelter gauge has an output voltage directly proportional to the heat flux with a sensitivity of $3.9 \pm 0.2 \text{ mV}/(\text{W}/\text{cm}^2)$ and a response time of approximately 250 ms. The diameter of the sensing area of the gauge is 3.18 mm. The output voltage from the Schmidt-Boelter gauge was amplified 1000 times and filtered by a 300-Hz low-pass filter. The signal was sampled at a frequency of 600 Hz and recorded by an IBM PC AT using a 12-bit Data Translation DT2801A A/D converter. The temperature of the gauge was measured by a T-type thermocouple mounted inside the gauge by the manufacturer.

Heat transfer coefficients were calculated from the measured gauge output by

$$h = \frac{E/S - \eta_g \sigma (T_g^4 - T_\infty^4)}{T_g - T_\infty} \quad (2)$$

The convection heat transfer coefficients were converted to nondimensional Stanton numbers, where the freestream velocity, C_p , and ρ were evaluated at the film temperature. The emissivity of the Microsensor was approximately 0. The emissivity of the Schmidt-Boelter gauge was 0.97.

Experimental Uncertainties

Uncertainties in the Stanton numbers were estimated at 20:1 odds using the methods described in Kline and McClintock.¹⁹ The major contributor to the uncertainty in Stanton number was the uncertainty in the static sensitivity of the heat flux gauges. The uncertainties in Stanton number were estimated to be 5.2 and 15.2% using the Schmidt-Boelter gauge and the Heat Flux Microsensor, respectively. Uncertainty in the sensor coordinates, x , z was 0.5 mm.

Experimental Results and Discussion

Experimental results are presented using the coordinate system shown in Fig. 1. Lengths are normalized using the distance from the model leading edge to the location of the primary separation line as measured from oil-flow visualizations and presented in Table 1. Note that this distance is different for each model. For the 3:2 elliptic nose/NACA 0020 tailed model, measurements were taken at the 60 locations along the seven lines shown in Fig. 3. The lines are numbered clockwise from the line of symmetry. Lines 1, 4, 6, and 7 correspond to the same locations where Devenport and Simpson¹ made 3-component velocity profile measurements. Measurements for the other two models were taken only along the centerline upstream of the model at the same locations where Ölçmen and Simpson² measured pressure fluctuations.

Mean Heat Flux

Mean heat flux measurements presented here were obtained from the Schmidt-Boelter gauge. Contours of constant Stanton number are shown in Fig. 3 for the modified NACA 0020 model. The Stanton numbers, nondimensionalized on freestream conditions, represent lines of constant heat transfer coefficient. The region of the flow close to the wing is an area of high heat flux created by the presence of the horseshoe vortex. This high heat flux is the result of both highly turbu-

lent mixing created by the vortex and cold freestream air transported by the vortex down the front of the wing perpendicular to the endwall. The locations of maximum levels of heat flux were close to the wing, at the wing/endwall junction. Upstream of the wing, the Stanton numbers approach the two-dimensional, zero pressure gradient boundary-layer Stanton number $St = 0.00184$, calculated using $StPr^{0.4} = 0.0287Re_x^{-0.2}$ and the estimated location of the virtual origin. The unheated starting length was negligible.

Distributions of mean surface heat flux on the centerline upstream of each model are shown in Fig. 4. From examining Fig. 4, it is apparent that the heat flux enhancement begins close to the separation line ($x/x_{sep} = -1.0$) for each model tested and that the heat flux in this region is produced by the secondary flow. Downstream of separation, the heat flux increases rapidly as the wing is approached, reaching a level almost 100% higher than in the approach boundary layer. This initial rise is followed by a plateau in the heat flux distributions. The heat flux levels attained here are approximately the same for the three models tested. For the modified NACA 0020 and the NACA 0015 models, this plateau appears to be centered around the line of low shear, at $x/x_{sep} = -0.60$ and $x/x_{sep} = -0.53$, respectively. An inflection point in the plot of Stanton number vs x/x_{sep} occurs just downstream of the line of low shear, approximately below the vortex center, followed by a second rapid increase in heat flux. The maximum value of Stanton number was found at the closest measurement location to the wing, where the maximum Stanton number measured was 0.0054, a 200% increase over the value of 0.0018 measured in the approach boundary layer. For the tapered cylinder model, the plateau in heat flux extends into the wing/endwall junction with no second rise in heat flux.

Heat Flux Fluctuations

Fluctuations in endwall surface heat flux presented here were measured using the Heat Flux Microsensor. The fluctuating component of heat flux measured along the centerline in front of each model is shown in Fig. 5. The fluctuations in heat flux increase rapidly after the separation line and reach a maximum value near the line of low shear. Fluctuations in heat flux decrease rapidly as the wing is approached. The fluctuating heat flux is a significant part of the total heat flux, reaching values as high as 25% of the mean heat flux near the line of low shear. The line of low shear has also been found to be the location of maximum level of pressure fluctuations^{2,3} and turbulence normal stresses.¹

Probability Density Functions

Distributions of the probability density function (pdf) of the heat flux fluctuations measured along the centerline in front of the modified NACA 0020 airfoil are shown in Fig. 6. The pdfs of heat flux fluctuations do not show the bimodal or "double-peaked" structure that have been found in the

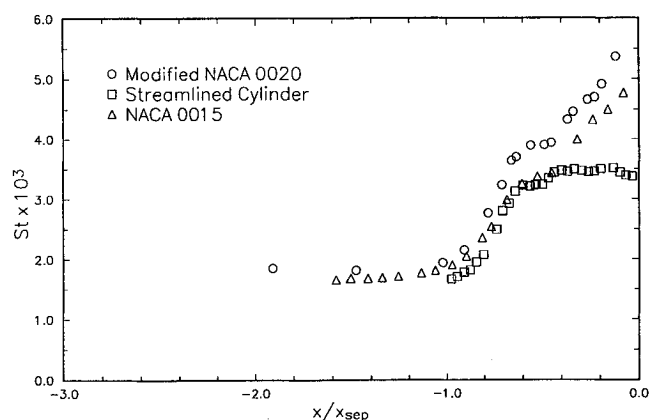


Fig. 4 Time-mean Stanton number distribution along the stagnation streamline for each model.

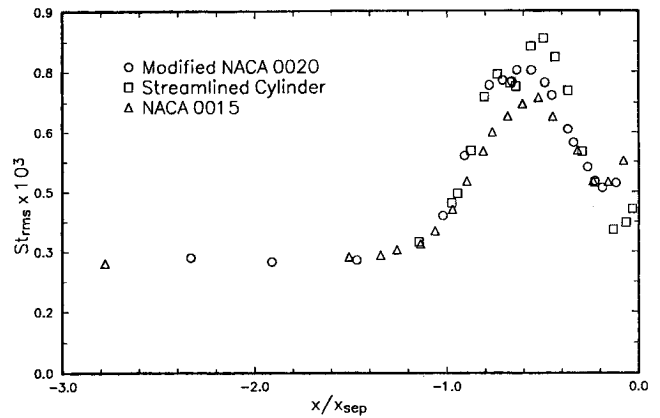


Fig. 5 Fluctuations in Stanton number measured along the stagnation streamline for each model.

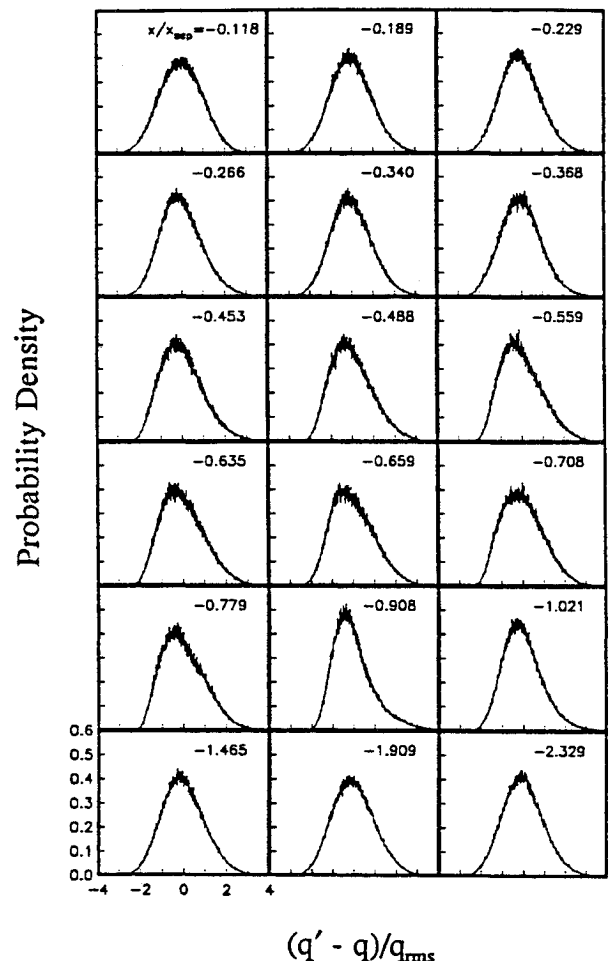


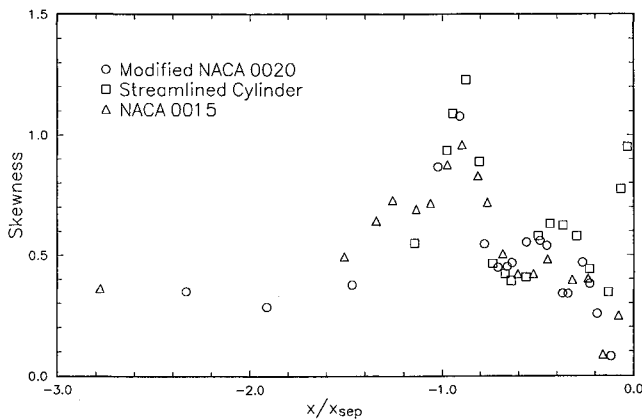
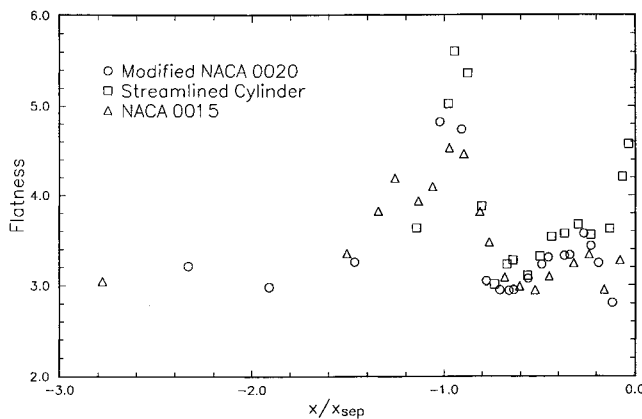
Fig. 6 Probability density functions of heat flux fluctuations measured on the stagnation streamline for the modified NACA 0020 wing.

velocity pdfs and in pdfs of pressure fluctuations measured on the endwall in front of the wing.

Although the heat flux pdfs are not bimodal, the effects of large scale unsteadiness are seen in the distortion of the pdfs. Distributions of the skewness and flatness factors of the heat flux pdfs are shown for each model in Fig. 7 and Fig. 8, respectively. For reference, a Gaussian pdf has a skewness equal to 0 and a flatness factor equal to 3. Maximum values of skewness and flatness of the heat flux pdfs were found in the vicinity of separation and are caused by the highly intermittent forward and reverse flow which exists in this region.¹ Table 2 presents the locations and values of the maximum mean Stanton number, rms Stanton number, skewness, and

Table 2 Location and value of maximum and minimum St , St_{rms} , skewness, and flatness

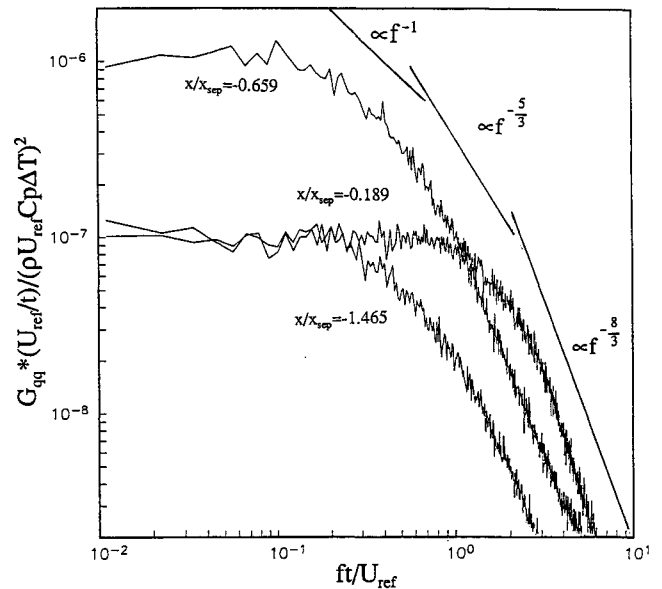
	Modified NACA 0020		Streamlined cylinder		NACA 0015	
	Value	x/x_{sep}	Value	x/x_{sep}	Value	x/x_{sep}
Maximum $St \times 10^3$	5.37	-0.118	3.51	-0.131	4.77	-0.078
Maximum $St_{rms} \times 10^3$	0.754	-0.636	0.833	-0.498	0.686	-0.524
Maximum skewness	1.08	-0.909	1.23	-0.876	0.96	-0.898
Maximum flatness	4.82	-1.022	5.61	-0.946	4.53	-0.973

**Fig. 7** Skewness factor of the heat flux pdfs for each model.**Fig. 8** Flatness factor of the heat flux pdfs for each model.

flatness for each wing. Upstream of the wing, in the approach boundary layer, the flatness approaches the Gaussian value of 3 and the skewness factor is approximately 0.35. The positive skewness in the approach boundary layer may be caused by the "sweeps" of high momentum, cold fluid from the outer region which occurs in the inner wall layer.

Power Spectra

One-sided autospectral density functions (power spectra) of the heat flux fluctuations were computed. Figure 9 presents a comparison of nondimensional spectra of the heat flux fluctuations measured in the approach boundary layer ($x/x_{sep} = -1.465$), in the region between the separation line and the vortex center ($x/x_{sep} = -0.659$), and near the wing/endwall junction ($x/x_{sep} = -0.189$) for the modified NACA 0020 wing. Frequency has been normalized by t/U_{ref} , which is the time it takes the freestream flow to travel one wing thickness. The spectra have been normalized by $(U_{ref}/t)(\rho U_{ref} C_p \Delta T)^2$ so that the area under the spectrum is equal to the variance of the local Stanton number. The spectra have been nondimensionalized in this way to allow direct comparison of spectral levels measured at different streamwise locations. Lines indicating the -1 and $-5/3$ power-law slopes for velocity fluctuation spectra²⁰ and a $-8/3$ power-law spectra are included in Fig. 9 for comparison.

**Fig. 9** Comparison of heat flux spectra measured in the approach boundary layer ($x/x_{sep} = -1.465$), in the region between the separation line and the line of low shear ($x/x_{sep} = -0.659$), and near the junction ($x/x_{sep} = -0.189$) for the modified NACA 0020 wing.

In general, the spectra have a region of almost constant spectral level at low frequencies followed by a rolloff with a $-8/3$ slope. While no spectra of heat flux fluctuations were available in the literature, the $-8/3$ power law has been found in the spectra for temperature fluctuations measured in fully developed pipe flow.²¹ Note that the results have not been corrected for the effects of the finite size of the heat flux sensor and that the spectra at high frequencies may be attenuated. Upstream of separation, in the approach boundary layer, the region of near constant spectral level extends up to a dimensionless frequency of $ft/U_{ref} = 0.3$, followed by the $-8/3$ rolloff. Downstream of separation, between the line of separation and the vortex center, there is a dramatic increase in spectral density, particularly at low frequencies. Further downstream, between the vortex center and the wing/endwall junction, there is an increase in spectral density at high frequencies.

The high levels of spectral density found in the region between the separation line and the vortex center are associated with the high heat flux fluctuations shown in Fig. 5. The high spectral levels at low frequencies suggest that the heat flux fluctuations in this region are created by large-scale, low-frequency, aperiodic, coherent motions. Spectra of the normal and streamwise velocity components measured by a laser-Doppler velocimeter in this region^{1,3} show a similarly dramatic increase in spectral density at low frequencies.

Near the wing/endwall junction, spectral energy exists at higher frequencies than elsewhere in the flowfield. At low frequencies, the spectral density levels are the same as in the approach boundary layer. However, the region of constant spectral density extends further, to a dimensionless frequency value of $ft/U_{ref} = 1.0$. This high-frequency energy could be the effect of a small counter-rotating vortex trapped in the junction, or the effect of small structures from the outer

boundary-layer region, transported by the main vortex, down the wing and into the junction.

From the results presented above and the available velocity data, a description of the augmentation in heat flux across the horseshoe vortex can be summarized by breaking the flowfield into three regions. In the first region, upstream of the line of separation, the heat flux is as would be expected for a two-dimensional, adverse pressure gradient boundary layer.

The second region, between the line of separation and the line of low shear, is dominated by the large-scale aperiodic motions of the horseshoe vortex. This region is characterized by highly intermittent forward and reverse flow. Turbulence energy production and turbulent stresses an order of magnitude higher than upstream were found in this region although surface shear stresses are small.¹ Mean heat flux levels are increased over upstream values by a factor of 2, and fluctuations of the heat flux are increased by a factor of 3. The augmentation in heat transfer in this region is due to turbulent mixing created by the unsteadiness of the recirculating flow.

Downstream of the line of low shear, in the third region, the heat flux increases rapidly and reaches a maximum value in the immediate vicinity of the wing/endwall junction while turbulence energy and fluctuations in heat flux decrease rapidly as the wing is approached. Skin friction values in this region are very large.²² The velocity field in this region is similar to an impinging jet. The fluid transported toward the endwall on the downwash side of the vortex impinges on the wing/endwall junction and is deflected radially in the spanwise direction and back upstream in a near wall jet of fluid. The heat flux in this region is determined by the effects of the vortex on the mean flow. The increase in heat flux in this third region is due to a thinning of the thermal boundary layer as cold fluid from the outer boundary layer or freestream is transported by the vortex to the near wall region.

This may explain the differences in mean heat flux in the near-wing region for each wing shown in Fig. 4. The time-mean heat flux in this near-wing region appears to be controlled by the size and location of the primary vortex. The size of the primary vortex is proportional to the location of the line of separation x_{sep} , which was 3.23, 2.71, and 6.59 cm for the modified NACA 0020, NACA 0015, and streamlined cylinder models, respectively. For the streamlined cylinder, the vortex is located much farther upstream, away from the wing than for the other two models. This may lead to a lower downwash velocity in the near-wing region for the streamlined cylinder model. Unfortunately, no detailed velocity data is available for this model to verify this conclusion.

Evaluation of St' Correlation

Since the heat flux rate outside of the line of low shear (in the first and second regions defined above) is believed to be primarily due to turbulence generated by the large-scale unsteadiness of the horseshoe vortex, one would expect a correlation between the turbulent stresses and the time-averaged heat flux. For two-dimensional boundary-layer flows, Maciejewski and Moffat²³ relate the local heat flux to the streamwise component of the turbulent normal stress through the use of a Stanton number based on $u_{rms,max}$ as

$$St' \equiv h/(\rho C_p u_{rms,max}) \quad (3)$$

where h is the local convection coefficient, and $u_{rms,max}$ is the maximum value of u_{rms} found in the boundary layer or freestream at the location where h is measured. Note that St' is not to be confused with St_{rms} , which is the nondimensional rms value of the fluctuations in heat flux. The St' correlation is of limited practical value since it requires a detailed knowledge of the turbulence structure that is usually not available. The authors use the St' correlation only 1) to demonstrate that the heat flux in this region is due to the turbulence field

and 2) to demonstrate that the St' correlation can be applied even to this complex, highly three-dimensional, separated flow.

Maciejewski and Moffat²³ suggest a functional form of the relation between St' and turbulence intensity $Tu = u_{rms,max}/U_{ref}$ for air ($Pr = 0.71$) as

$$St' = 0.0184 + 0.0092 \exp - [(Tu - 0.11)/0.055]^2 \quad (4)$$

This form has a peak value at a turbulence level of 11%. For turbulence intensities above 0.20, $St' \approx 0.0184$. Maciejewski and Moffat applied this correlation to heat flux experiments for various complex flow situations from the literature and found Eq. (4) to be valid to within 15% at (20:1) odds independent of flow geometry or Reynolds number.

To extend the St' correlation to three-dimensional flows, the authors chose to substitute the maximum value of turbulent kinetic energy present in the boundary layer $k_{rms,max}$ in place of $u_{rms,max}$ in Eq. (3). The value of $k_{rms,max}/U_{ref}$ was obtained from the LDV data of Devenport and Simpson,¹ which were measured at a freestream velocity of 27 m/s and an approach Reynolds number based on momentum thickness of 6700. This value of $k_{rms,max}/U_{ref}$ may not be the same as the value of $k_{rms,max}/U_{ref}$ for the present data for which $U_{ref} = 32.3$ m/s and $Re_\theta = 3700$. It is assumed, however, that $k_{rms,max}/U_{ref}$ is not a strong function of Reynolds number for this flow. This assumption is supported by the fact that the locations of the line of low shear and the line of separation revealed by the oil flow visualizations performed at the lower Reynolds number² were found to agree with the locations of these lines obtained from oil flow visualizations of Devenport and Simpson.¹ This suggests that the size and location of the primary vortex, and presumably the turbulence structure, is the same for the flowfield of Devenport and Simpson and the flowfield of the current study.

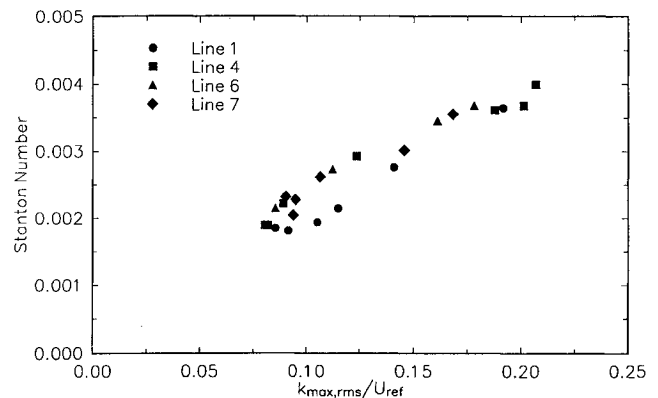


Fig. 10 Relation between heat flux and $k_{rms,max}$ in the region outside of the line of low shear for the modified NACA 0020 wing.

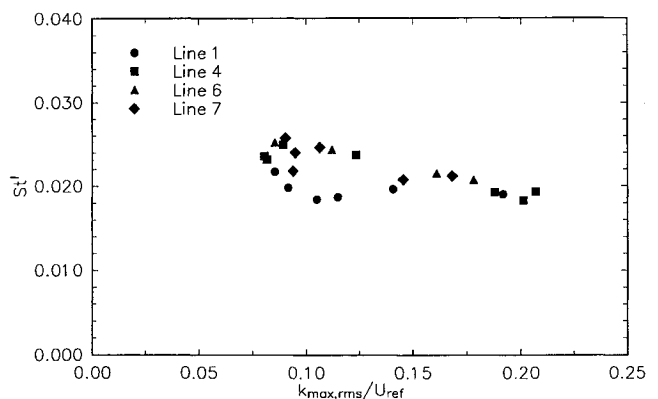


Fig. 11 St' correlation for heat flux in the region outside of the line of low shear for the modified NACA 0020 wing.

Figure 10 shows the local heat transfer coefficient as a function of $k_{\max,\text{rms}}/U_{\text{ref}}$ for data measured along lines 1, 4, 6, and 7. Only data from regions I and II, outside of the line of low shear, were used. The heat flux in this region varies by a factor of 2.5. A linear relation is seen to exist between St and $k_{\max,\text{rms}}/U_{\text{ref}}$. St' correlations were computed from the heat transfer coefficients in Fig. 10, and are shown as a function of $k_{\max,\text{rms}}/U_{\text{ref}}$ in Fig. 11. The values of St' have a mean value of 0.0217 and a standard deviation of 11%. A peak in St' does seem to appear around a turbulence level of 10%.

Conclusions

Time- and spatially-resolved heat flux measurements have been made on the endwall surface in a wing/body junction vortex system. Both the time-averaged and fluctuating components of the heat flux have been examined. The time-averaged heat flux was found to have a maximum value in the immediate vicinity of the wing. This high level of heat flux in the region adjacent to the wing is due to the effect of the junction vortex on the mean velocity field. The position of the primary vortex center, and therefore the wing shape, was found to strongly affect the level of heat flux in this region.

Further upstream, between the separation line and the line of low shear, the time-averaged heat flux was found to be related to the high levels of turbulence stresses produced by the bimodal switching of the velocity field. The heat flux measured in this region was related to the turbulent stresses using a three-dimensional extension of the St' correlation of Maciejewski and Moffat.

It was found that the line of low shear and the maximum value of fluctuations in heat flux q_{rms} occur at the same location. Histograms of the heat flux fluctuations were highly distorted in the region surrounding the separation line although no bimodal structure was found. Maximum values of skewness and flatness of the histograms of surface heat flux were located near the line of separation. Spectra of the heat flux fluctuations showed high levels of low-frequency energy in this region.

Acknowledgments

The authors gratefully acknowledge support for this research from the U.S. Air Force Office of Scientific Research through Grant AFOSR-91-0310 under the supervision of Dan Fant, Program Manager. The authors would like to thank Magali Tollard and Karen Baker for their help in taking some of the measurements, and S. M. Ha for taking the hot-wire measurements.

References

- ¹Devenport, W. J., and Simpson, R. L., "Time-Dependent and Time-Averaged Turbulence Structure Near the Nose of a Wing-Body Junction," *Journal of Fluid Mechanics*, Vol. 210, Jan. 1990, pp. 23–55.
- ²Ölçmen, S. M., and Simpson, R. L., "Influence of Wing Shapes on the Surface Pressure Fluctuations of a Wing-Body Junction," *AIAA Journal*, Vol. 32, No. 1, 1994, pp. 6–15.
- ³Rife, M. C., "An Experimental Study of the Relationship Between Velocity and Pressure Fluctuations in a Wing-Body Junction," M.S. Thesis, Aerospace and Ocean Engineering Dept., Virginia Polytechnic Inst. and State Univ., Blacksburg, VA, 1992.
- ⁴Kim, S., "Observation and Measurement of Flow Structures in the Stagnation Region of a Wing-Body Junction," Ph.D. Dissertation, Aerospace and Ocean Engineering Dept., Virginia Polytechnic Inst. and State Univ., Blacksburg, VA, 1991.
- ⁵Blair, M. F., "An Experimental Study of Heat Transfer and Film Cooling on Large-Scale Turbine Endwalls," *Journal of Heat Transfer*, Vol. 96, No. 4, 1974, pp. 524–529.
- ⁶Dunn, M. G., and Stoddard, F. J., "Measurement of Heat-Transfer Rate to a Gas Turbine Stator," *Journal of Engineering for Power*, Vol. 101, April 1979, pp. 275–280.
- ⁷Graziani, R. A., Blair, M. F., Taylor, J. R., and Mayle, R. E., "An Experimental Study of Endwall and Airfoil Surface Heat Transfer in a Large Scale Turbine Blade Cascade," *Journal of Engineering for Power*, Vol. 102, No. 2, 1980, pp. 257–267.
- ⁸Georjoui, D. P., Godard, M., and Richards, B. E., "Experimental Study of the Iso-Heat-Transfer-Rate Lines on the End-Wall of a Turbine Cascade," American Society of Mechanical Engineers Paper 79-GT-20, March 1979.
- ⁹Gaugler, R. E., and Russell, L. M., "Comparison of Visualized Turbine Endwall Secondary Flows and Measured Heat Transfer Patterns," American Society of Mechanical Engineers Paper 83-GT-83, March 1983.
- ¹⁰Hylton, L. D., Mihelc, M. S., Turner, E. R., and York, R. E., "Experimental Investigation of the Turbine Endwall Heat Transfer," Air Force Wright Aeronautical Labs., AFWAL-TR-81-2077, 3 Vols., 1981.
- ¹¹Hippensteele, S. A., and Russell, L. M., "High-Resolution Liquid-Crystal Heat-Transfer Measurements on the End Wall of a Turbine Passage with Variations in Reynolds Number," NASA TM 100827, July 1988.
- ¹²Swisher, S. E., Diller, T. E., and Pierce, F. J., "Time-Resolved Heat Flux Measurements in a Turbulent Junction Vortex," *Topics in Heat Transfer*, edited by M. Keyhani et al., Vol. 1, American Society of Mechanical Engineers, New York, 1992, pp. 55–63.
- ¹³Kays, W. M., and Crawford, M. E., *Convection Heat and Mass Transfer*, 2nd ed., McGraw-Hill, New York, 1980, pp. 213–217.
- ¹⁴Lewis, D. J., Simpson, R. L., and Diller, T. E., "Time-Resolved Surface Heat Flux Measurements in the Wing/Body Junction Vortex," AIAA Paper 93-0918, Jan. 1993.
- ¹⁵Simmons, S. G., Hager, J. M., and Diller, T. E., "Simultaneous Measurements of Time-Resolved Surface Heat Flux and Freestream Turbulence at a Stagnation Point," *Heat Transfer 1990*, edited by G. Hetsroni, Vol. 2, Hemisphere, New York, 1990, pp. 375–380.
- ¹⁶Hager, J. M., Terrell, J. P., Langley, L. W., Onishi, S., and Diller, T. E., "Measurements with the Heat Flux Microsensor," *Proceedings of the 37th International Instrumentation Symposium*, Instrument Society of America, Research Triangle Park, NC, 1991, pp. 551–561.
- ¹⁷Hager, J. M., Simmons, S., Smith, D., Onishi, S., Langley, L. W., and Diller, T. E., "Experimental Performance of a Heat Flux Microsensor," *Journal of Turbomachinery*, Vol. 113, No. 2, 1991, pp. 246–250.
- ¹⁸Baker, K., "Unsteady Surface Heat Flux and Temperature Measurement," M.S. Thesis, Mechanical Engineering Dept., Virginia Polytechnic Inst. and State Univ., Blacksburg, VA, 1993.
- ¹⁹Kline, S. J., and McClintock, F. A., "Describing Uncertainty in Single Sample Experiments," *Mechanical Engineering*, Vol. 75, No. 1, 1953, pp. 3–8.
- ²⁰Townsend, A. A., *The Structure of Turbulent Shear Flow*, 2nd ed., Cambridge Univ. Press, Cambridge, England, UK, 1976, pp. 93–99.
- ²¹Hishida, M., and Nagano, Y., "Structure of Turbulent Velocity and Temperature Fluctuations in Fully Developed Pipe Flow," *Journal of Heat Transfer*, Vol. 101, No. 1, 1979, pp. 15–22.
- ²²Devenport, W. J., and Simpson, R. L., "Time-Dependent Structure in Wing-Body Junction Flows," *Turbulent Shear Flows 6*, Springer Verlag, Berlin, 1989, pp. 232–248.
- ²³Maciejewski, P. K., and Moffat, R. J., "Heat Transfer with Very High Turbulence Free-Stream Turbulence: Part II—Analysis of Results," *Journal of Heat Transfer*, Vol. 114, No. 4, 1992, pp. 834–839.